RSC Advances

PAPER

View Article Online
View Journal | View Issue

Cite this: *RSC Adv.*, 2017, **7**, 31287

Facile synthesis of nanocrystalline-assembled nest-like NiO hollow microspheres with superior lithium storage performance†

Yanwei Li,*[a] Yuanyuan Zheng,[a] Jinhuan Yao,*[a] Jianrong Xiao,[b] Jianwen Yang[a] and Shunhua Xiao[a]

Received 12th May 2017
Accepted 12th June 2017

DOI: 10.1039/c7ra05373h

rsc.li/rsc-advances

Interconnected nest-like NiO hollow microspheres assembled from nanocrystallites are prepared by a facile hydrothermal method followed by annealing at 700 °C in air. It is noteworthy that the NiO hollow microspheres exhibit a very significant pseudocapacitive effect which makes a great contribution to the enhanced lithium storage performance. Benefiting from the advantages of unique nest-like nanoarchitecture and pseudocapacitive effect, the NiO hollow microspheres show high reversible capacity, superior cyclic performance, and excellent high rate capability. When used as anode materials for lithium ion batteries, the NiO hollow microspheres maintain a capacity of 650 mA h g^{-1} after 100 cycles at a current density of 1 A g^{-1}. The capacity retention is 93%, which corresponds to a very small capacity decay of 0.07% per cycle. In particular, even at an ultra-high current density of 10 A g^{-1}, the NiO electrode still delivers a stable discharge capacity of 457 mA h g^{-1}.

1. Introduction

As a type of highly efficient energy storage system, lithium ion batteries (LIBs) have been widely used as power sources in portable electronic devices, stationary energy storage systems, and rapidly developing electric vehicles (EVs).[1,2] However, the commercial graphite anode materials in LIBs suffer from low theoretical capacity (372 mA h g^{-1}) and poor rate capability, which cannot meet the increasing requirement for more demanding applications due to the limitations in energy capacity and reliable operation.[3,4] Therefore, it is essential to develop alternative high-capacity anode materials for the next-generation LIBs.

In recent years, transition metal oxides are considered as the potential candidates for the next generation anode materials for LIBs because of their large specific capacity, high volumetric energy density, safety, and much improved rate capability than those of conventional graphite anodes.[5,6] Among those transition mental oxides, nickel oxide (NiO) has been focused on as one of the most promising anode materials for LIBs because of its high theoretical capacity (718 mA h g^{-1}), high volumetric energy density, natural abundance, low cost, low toxicity, and superior safety.[7,8] However, the pulverization of NiO particles associated with repeatedly volume expansion and contraction during lithiation/delithiation cycles leads to large irreversible capacity loss and poor cycling stability, which greatly limits its practical application in LIBs.[9,10] A promising solution is to reduce the size of active materials to nanoscale, which can not only shorten the diffusion pathway of both lithium ions and electrons, but also effectively relieve the pressure derived from the volume changes during discharge/charge cycles.[11,12] Among various nanostructures, micro/nano-structured hollow spheres have received great attentions due to their unique structural features, fascinating physicochemical properties, and widespread applications.[13,14] Hollow micro/nano structures could effectively accommodate the severe volume variation of electrode materials upon cycling and prevent self-aggregation of the nanoscale subunits, which could alleviate the pulverization of active materials and significantly improve the cycling performance.[15] In addition, the hollow micro/nano structures facilitate electrolyte penetration and provide large contact area between the electrode and the electrolyte; the nanosized primary building blocks could ensure short transport length for both lithium ions and electrons, resulting in enhanced rate capability.[13] For example, Huang *et al.*[16] synthesized NiO hollow microspheres by co-hydrolysis of nickel nitrate and tetraethyl orthosilicate in an ammonia solution and subsequent calcination and HF treatment processes, which showed a reversible capacity of 560 mA h g^{-1} after 40 cycles at 0.2 A g^{-1}. Wang *et al.*[17] fabricated NiO hollow spheres with size of ~2 μm using carbon microspheres as template and it delivered a capacity of 598 mA h g^{-1} after 50 cycles at 0.2 A g^{-1}. However, the synthesis procedures and reactant materials for fabricating these hollow

[a]*Guangxi Key Laboratory of Electrochemical and Magneto-chemical Functional Materials, College of Chemistry and Bioengineering, Guilin University of Technology, Guilin 541004, China. E-mail: lywhit@126.com; yaojinhuan@126.com; Fax: +86 773 5896839; Tel: +86 773 2538354*

[b]*College of Science, Guilin University of Technology, Guilin, 541008, China*

† Electronic supplementary information (ESI) available. See DOI: 10.1039/c7ra05373h

structured materials are usually complex and expensive; the sizes of products are always as large as several micrometers resulting in lower volumetric energy density.

In the present work, we report a facile and cost-effective method to synthesize interconnected nest-like NiO hollow microspheres (only ~1 μm) composed of nanosized primary particles (~50 nm). When tested as anode materials for LIBs, the interconnected nest-like hollow structures endow NiO microspheres with excellent electrochemical performance. In particular, we analyze the lithium storage mechanism of the NiO hollow microspheres, and found that pseudocapacitive effect has a great contribution to the high capacity and good rate capability, providing a new approach to design and optimize micro/nano electrode materials with superior rate performance.

2. Experimental

2.1. Synthesis of interconnected nest-like NiO hollow microspheres

Interconnected nest-like NiO hollow microspheres were prepared by a two-step approach of hydrothermal synthesis of spherical $Ni(HCO_3)_2$/C precursor and subsequent heat treatment in air. All the chemical agents were analytical grade and used without further purification. In a typical synthesis procedure of precursory $Ni(HCO_3)_2$ microspheres, 4.16 g nickel chloride ($NiCl_2 \cdot 6H_2O$), 4.2 g urea (NH_2CONH_2), 4.0 g glucose ($C_6H_{12}O_6$) were dissolved in 70 mL deionized water under vigorous stirring. Then, the blue solution was transferred into a Teflon-lined stainless steel autoclave. It was maintained at 180 °C for 4 h and then cooled naturally to room temperature. The resultant gray black $Ni(HCO_3)_2$/C microspheres were filtered, rinsed with deionized water three times, and freeze dried until constant weight. Finally, nest-like NiO hollow microspheres were obtained by calcining the precursor of $Ni(HCO_3)_2$/C microspheres at 700 °C for 3 h in a muffle furnace with a rate of 5 °C min^{-1} in air.

2.2. Physical characterizations

The phase structures of the prepared samples were analyzed by X-ray diffraction (XRD) on a X'Pert[3] diffractometer (PANalytical, Netherlands) with Cu Kα radiation ($\lambda = 1.54056$ Å) over the range of 10° to 90° (2θ) with a scanning speed of 5° min^{-1}. The morphologies and microstructures of the interconnected nest-like NiO hollow microspheres were characterized by Hitachi SU-5000 field emission scanning electron microscope (FESEM) and JEM-2100Plus high resolution transmission electron microscope (HRTEM) with an operating voltage of 200 kV. The thermogravimetric analysis (TGA) was performed on a TGA Q500 thermal analyzer at a ramp of 5 °C min^{-1} in air from room temperature to 800 °C. The nitrogen adsorption and desorption isotherms were measured at 77 K on a Micromeritics Tristar 3020 analyzer.

2.3. Electrochemical measurements

The working electrode was prepared by mixing the active material (the NiO hollow microspheres), conductive additive (Super-P), and polymer binder (PVDF) in *N*-methyl pyrrolidinone (NMP) solvent with a weight ratio of 6 : 3 : 1. The resultant slurry was then uniformly coated on a copper foil and dried in a vacuum oven at 80 °C for 12 h. Afterward, the electrodes were punched into disks and assembled into CR2016 coin type cells in an high purity Ar gas filled glove box with metal lithium sheets as the counter electrode and the reference electrode, Celgard 2400 film as separator, and 1 M $LiPF_6$ in a non-aqueous solution of ethylene carbonate (EC), diethyl-carbonate (DEC) and dimethyl carbonate (DMC) (1 : 1 : 1 by volume) as electrolyte. The thickness, diameter, and mass loading of the working electrode were 8.34 μm, 15.0 mm, and ~0.8 mg, respectively. Cyclic voltammetry (CV) was measured using an electrochemical workstation (CHI760E) within the voltage range from 0.01 V to 3.0 V (*vs.* Li/Li^+). Electrochemical impedance spectroscopy (EIS) was conducted on electrochemical workstation (CHI760E) at a frequency range that varied from 10 mHz to 100 kHz with an AC signal amplitude of 5 mV at open-circuit potential (OCP) in a fully charged state. The discharge/charge cycling performance was tested on the Neware BTS-5 V/10 mA multi-channel battery testing system between 0.01 V and 3.0 V *vs.* Li^+/Li. All measurements above were carried out at room temperature (25 °C).

3. Results and discussion

3.1. Structure analysis of the prepared samples

Fig. 1a shows the XRD pattern of the precursor before annealing in air. All the diffraction peaks are well-matched

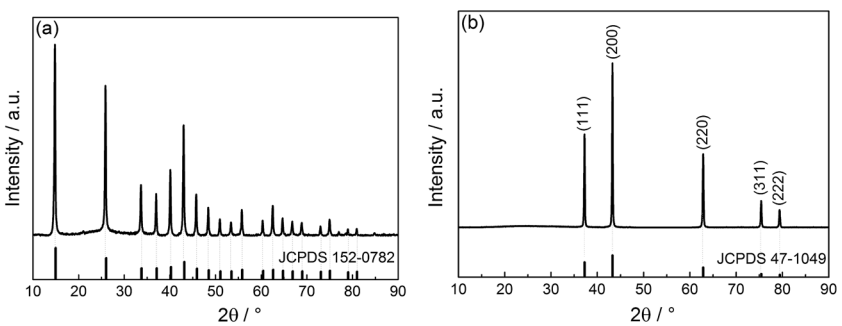

Fig. 1 XRD patterns of the NiO precursor (a) before and (b) after annealing. The vertical lines at the bottom are the standard diffraction peaks of $Ni(HCO_3)_2$ (JCPDS 152-0782) and NiO (JCPDS 47-1049).

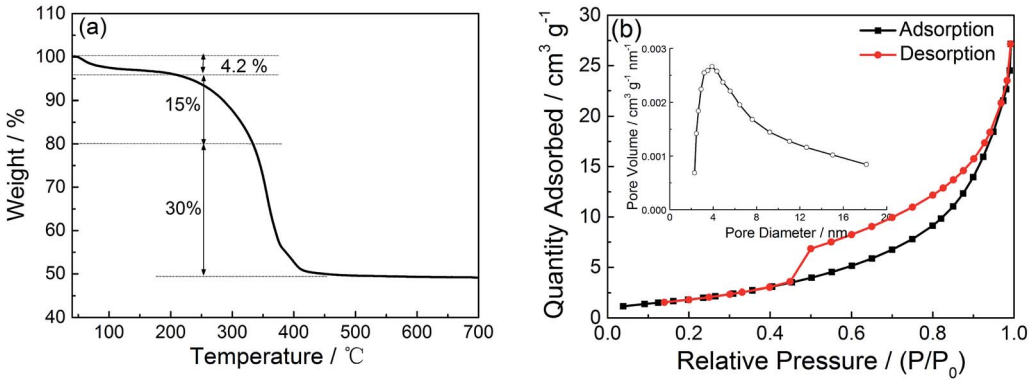

Fig. 2 (a) TGA plot of the NiO precursor and (b) nitrogen adsorption/desorption isotherm curves (inset: BJH pore size distribution of corresponding sample) for the interconnected nest-like NiO hollow microspheres.

with the $Ni(HCO_3)_2$ (JCPDS 152-0782).[18] The strong and narrow peaks suggest that the as-synthesized $Ni(HCO_3)_2$ is of high crystallinity. No diffraction peaks of carbon are observed because the carbon is in the amorphous state. Fig. 1b gives the XRD pattern of the final sample prepared by annealing the precursor at 700 °C for 3 h in air. The five strong and well defined diffraction peaks at 37.12°, 43.16°, 62.77°, 75.30°, and 79.29° are perfectly indexed to the (111), (200), (220), (311), (222) planes of face-centered cubic NiO phase (JCPDS 47-1049), respectively. No other diffraction peaks are observed, indicating that the precursor has completely converted to the cubic phase NiO after annealing in air. The average crystallite size calculated using the Scherrer equation is about 50 nm, which is in good accordance with the TEM examination (Fig. 3f).

Fig. 2a presents the TGA plot of the precursor tested in air atmosphere. The first weight loss of 4.2 wt% from 25 to 200 °C indicates the loss of adsorbed water molecules. The weight loss of 15 wt% from 200 °C to 340 °C can be ascribed to oxidation of carbon microspheres.[19] The sharp weight loss of 30% from 350 °C to 450 °C can be attributed to the decomposition of $Ni(HCO_3)_2$.[18] With the temperature increasing from 450 °C to 700 °C, the TGA curve almost remains, implying that the precursor has been completely converted to NiO. The Brunauer–Emmett–Teller (BET) surface area of the NiO sample is characterized by nitrogen adsorption/desorption isotherms at 77 K. As shown in Fig. 2b the isotherm profile of the sample exhibits a typical type IV curve with a H3 hysteresis loop, suggesting the existence of a large number of mesopores in the NiO sample. The BET surface area is 7.9 $m^2\ g^{-1}$. Through Barrett–Joyner–Halenda (BJH) analysis (inset in Fig. 2b), the pore size distribution ranges from 2 to 18 nm and the dominant peak is at 4 nm, suggesting the mesoporous nature of the NiO hollow microspheres. The result is in accordance with the HRTEM images as shown in Fig. 3f and g. The mesopores in NiO sample may benefit the penetration of electrolyte into NiO and diffusion of Li^+ into active sites with less resistance, and in addition can buffer the large volume expansion during discharge/charge cycles.

Fig. 3 presents the SEM images of the precursor and as-prepared NiO sample. As shown in Fig. 3a and b, it is observed that the precursor is composed of interconnected microspheres with a rough surface. After the annealing treatment, the precursor transforms into interconnected nest-like hollow microspheres (Fig. 3c and d). The shell of the NiO hollow microspheres is assembled from small nanoparticles. Fig. S1† shows the average diameter of the NiO hollow microspheres is about 1 μm. To better illustrate the structure and porosity of the as-prepared NiO sample, representative TEM images are shown in Fig. 3e and f. Fig. 3e further evidences that all the microspheres have a hollow interior and interconnect with adjacent ones. The average size of the primary building blocks in the NiO hollow microspheres observed from the TEM image (Fig. 3f) is about 50 nm, which is consistent with the XRD results. The HRTEM image shown in Fig. 3g reveals the clear lattice fringes of the NiO nanoparticles with a lattice interplanar spacing of 0.15 nm, which corresponds to the (220) crystal plane of NiO and is also well consistent with the XRD results. The corresponding selected area electron diffraction (SAED, Fig. 3h) pattern displays five diffraction rings assigned to the (111), (200), (220), (311), and (222) planes, respectively, indicating the polycrystalline nature of the NiO hollow microspheres.

Based on the above analysis, the preparation process of the interconnected nest-like NiO hollow microspheres is illustrated in Fig. 4. In this preparation process, glucose is first hydrothermal polymerized and carbonized to form carbon microspheres under hydrothermal condition.[20] The presence of many hydrophilic oxygen-containing functional groups (particularly hydroxyl and carboxyl groups) on the surface of carbon microspheres provide abundant negative-charged active sites to adsorb Ni^{2+}.[20] The gradually generated HCO_3^- from urea decomposition reacts with the adsorbed Ni^{2+} on the surface of the carbon microspheres and forms $Ni(HCO_3)_2$ coating layer by Ostwald ripening (as illustrated in eqn (1)–(5)).[21,22] Finally, interconnected nest-like porous NiO hollow microspheres can be obtained after a simple annealing of $Ni(HCO_3)_2$/C precursor in air. The following reactions are involved in the formation of $Ni(HCO_3)_2$ and NiO.

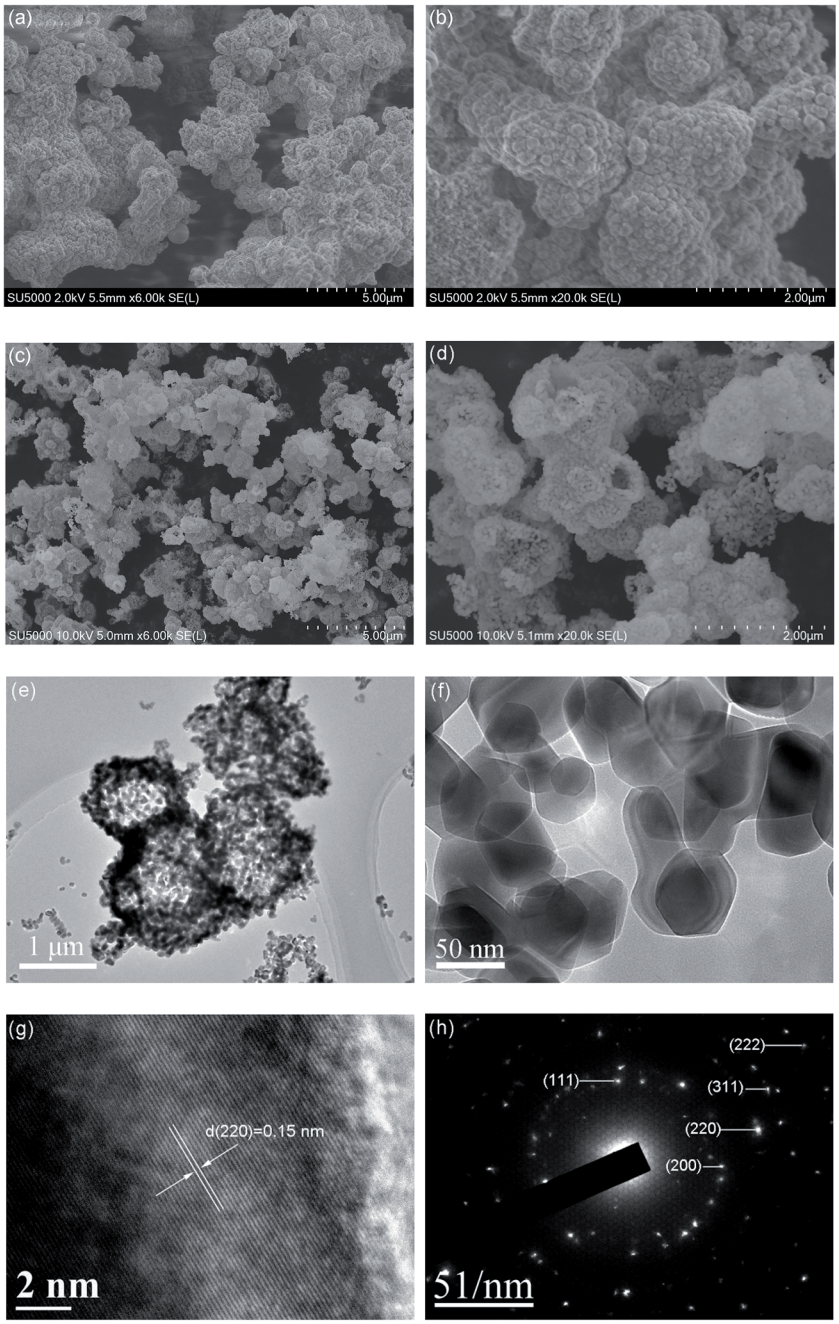

Fig. 3 SEM images of the NiO precursor (a and b) and the NiO hollow microspheres (c and d). TEM images (e and f), HRTEM image (g) and SAED pattern (h) of the NiO hollow microspheres.

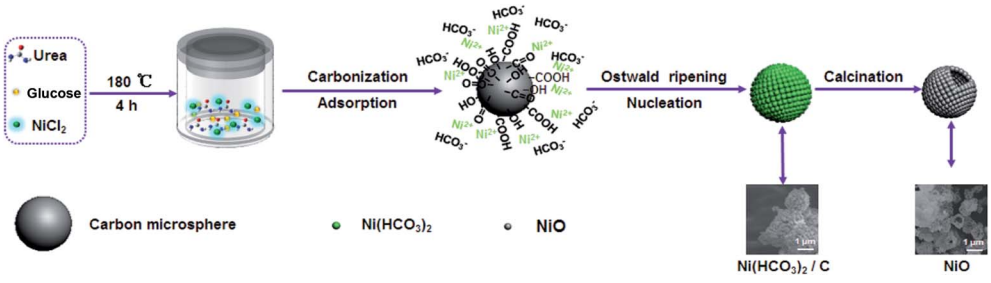

Fig. 4 Possible formation mechanism of the NiO hollow microspheres.

$$CO(NH_2)_2 + H_2O \rightarrow 2NH_3 + CO_2\uparrow \quad (1)$$

$$NH_3\cdot H_2O \rightarrow NH_4^+ + OH^- \quad (2)$$

$$CO_2 + 2OH^- \rightarrow CO_3^{2-} + H_2O \quad (3)$$

$$CO_3^{2-} + H_2O + CO_2 \rightarrow 2HCO_3^- \quad (4)$$

$$Ni^{2+} + 2HCO_3^- \rightarrow Ni(HCO_3)_2\downarrow \quad (5)$$

$$Ni(HCO_3)_2 \rightarrow NiO + 2CO_2\uparrow + H_2O\uparrow \quad (6)$$

3.2. Electrochemical performance of the prepared samples

Fig. 5a gives the CV curves of the interconnected nest-like NiO hollow microspheres at the initial four scanning cycles. In the first CV cycle, the intense irreversible cathodic peak at 0.50 V can be ascribed to the initial reduction of Ni^{2+} to Ni^0, the generation of Li_2O matrix, and the formation of the solid electrolyte interface (SEI) layer on the surface of electroactive materials;[23] the oxidation peak at about 2.16 V corresponds to the reversible oxidation of Ni^0 to Ni^{2+}, decomposition of Li_2O to Li, and the partial dissolution of SEI.[7,9] In the second CV cycle, the shift of reduction and oxidation peaks to 1.31 V and 2.23 V from 0.50 V and 2.16 V, respectively, are due to the drastic lithium-driven structural or textural modifications.[8,24] After the second cycle, the CV profiles are almost overlapped each other, suggesting a good electrochemical reversibility and a cyclic stability of the synthesized NiO hollow microspheres.[10]

Fig. 5b gives the galvanostatic discharge/charge curves of the interconnected nest-like NiO hollow microspheres for the 1st, 2nd, 5th, 15th, 50th, 80th, and 100th cycle at a current density of 1 A g^{-1} in the voltage range of 0.01–3.0 V. For the first discharge, there exists a long potential plateau at ~0.50 V corresponding to the reduction of Ni^{2+} to Ni^0 and the formation of Li_2O and solid electrolyte interface (SEI) film.[23] The initial discharge/charge capacities are 1190/753 mA h g^{-1}, and the corresponding coulombic efficiencies is 63.2%. This obvious coulombic

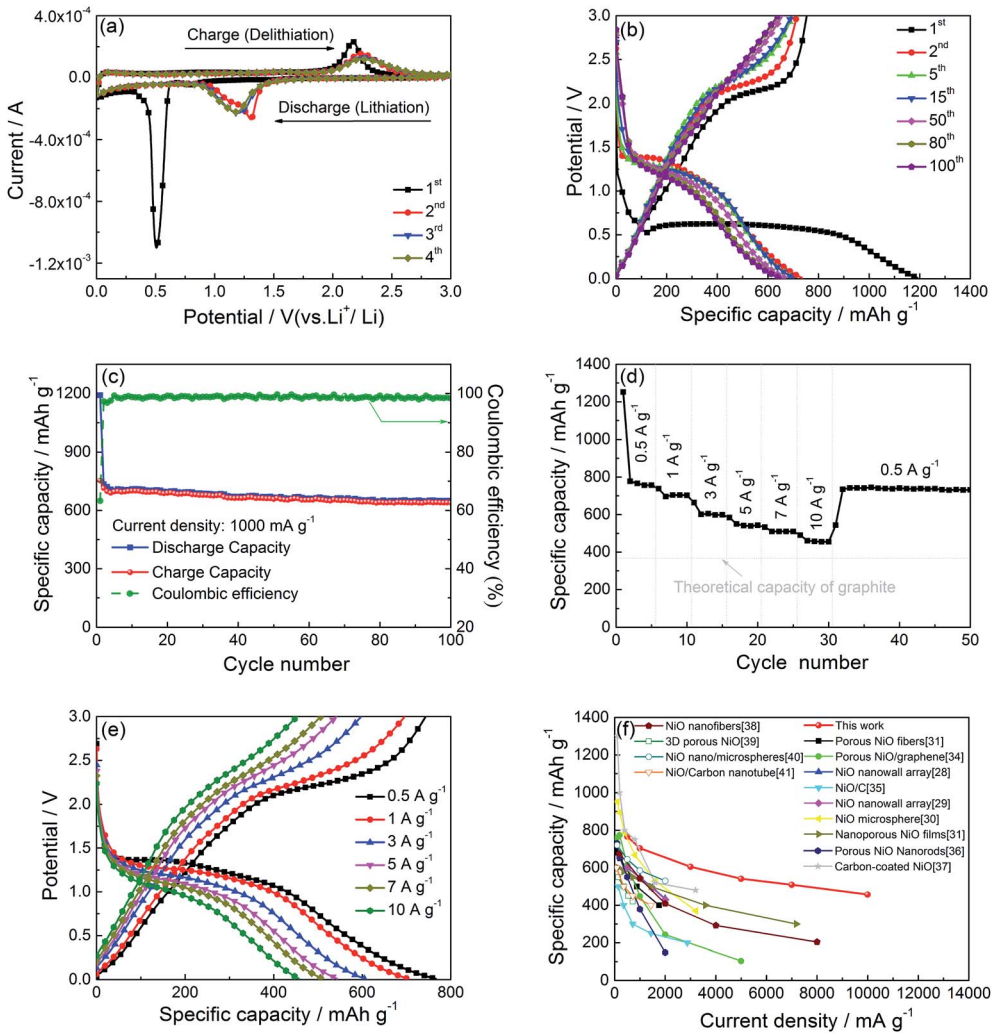

Fig. 5 (a) CV curves at 0.1 mV s^{-1}, (b) discharge/charge voltage profiles at 1000 mA g^{-1}, (c) cyclic performance at 1000 mA g^{-1}, (d) rate performance at different current density, and (f) the representative discharge/charge voltage profiles at various rates of the NiO hollow microspheres electrode. (e) Comparison of the rate capabilities with previous reported NiO-based materials.

Table 1 Comparison of the lithium storage performance of the interconnected nest-like NiO hollow microspheres electrode to reported NiO-based materials

Samples	Current density (mA g^{-1})	Capacity retention (mA h g^{-1})	Ref.
NiO hollow microspheres	1000	650 after 100 cycles	This work
Porous NiO film	71.8	570 after 40 cycles	26
Nano-NiO particles	718	592 after 50 cycles	27
NiO nanowall array	300	567 after 50 cycles	28
NiO nanowall array	500	564 after 50 cycles	29
NiO microsphere	502	597 after 100 cycles	30
Nanoporous NiO films	143	543 after 100 cycles	31
NiO nanoflakes	50	411 after 20 cycles	32
Ni-coated NiO	100	640 after 50 cycles	33

inefficiency at the first cycle can be ascribed to the presence of side reactions, such as irreversible electrolyte decomposition and formation of SEI layer,[8,10] which is common in most transition metal oxides.[5,6,25] From the second cycle onward, the discharge plateau shifts to 1.0–1.3 V, while the charge plateau slightly shifts to higher potential, which is consistent with the CV results. In particular, the charge potential plateau almost disappears in the 100th cycle.

Fig. 5c shows the cycling performance and coulombic efficiency of the NiO electrode at a current density of 1 A g^{-1} in the voltage range of 0.01–3.0 V. The formation of SEI layer on the electrode materials leads to low coulombic efficiency at the first cycle. After the initial 5 cycles, the coulombic efficiency drastically increases up to 98%. After 100 cycles, the NiO electrode can still delivers a discharge capacity of 650 mA h g^{-1}, and the capacity retention is 92.86% compared to the 5th cycle. The discharge capacity and cycling stability are much superior to the previous reported NiO-based electrode materials (as listed in Table 1).

The rate capability of the interconnected nest-like NiO hollow microspheres is presented in Fig. 5d. The stable discharge capacities of the NiO hollow microspheres at current densities of 0.5, 1, 3, 5, and 7 A g^{-1} are around 766, 704, 605, 541, and 509 mA h g^{-1}, respectively. When cycled at even the high rate of 10 A g^{-1}, a capacity of 457 mA h g^{-1} can be still maintained, which is much higher than the theoretical capacity of graphite (378 mA h g^{-1}). Furthermore, while the current density jumps back to the 1 A g^{-1}, the discharging capacity recovers to the value of around 740 mA h g^{-1}. The above results demonstrate that the NiO hollow microspheres have excellent rate performance, high reversibility, and stability for high power LIBs. Fig. 5e gives the selected discharge/charge voltage profiles of the NiO hollow microspheres at various current densities. It can be seen that with the increase of current densities, the discharge voltage decreases and the charge voltage increases due to the increasing polarization effect.[8] However, even under ultrahigh current densities, such as 7 A g^{-1} and 10 A g^{-1}, these discharge and charge plateaus can still be well distinguished, suggesting the outstanding high-rate performance. The rate capability of this NiO hollow microspheres is obviously better than those previous reported NiO-based electrode materials as shown in Fig. 5f.

To better understand the superior electrochemical performance of the NiO hollow microspheres, EIS measurements are performed on the electrode before and after the 1st, 5th, 15th, 35th, 60th, 80th, and 100th cycle and the results are shown in Fig. 6. All EIS experiments are performed in the charged state at open-circuit potential (OCP). Before discharge/charge process, the spectrum is composed of one depressed semicircles in the high-frequency region and a sloped line in the low-frequency region (Fig. 6a). The depressed semicircle in the high-frequency region reflects the charge transfer resistance (R_{ct}) between the electrode and the electrolyte, while the sloped line in the low-frequency region is related to the lithium ion diffusion impedance.[42–44] In the initial 15 cycles, only one depressed semicircle is observed in the high to medium frequency range suggesting that the effects due to surface film and charge transfer are not separable. In this case, the combined process of surface film resistance (R_{sf}) and the charge transfer resistance (R_{ct}) could be assigned as R_{sf+ct}. These Nyquist plots are fitted with the equivalent circuit shown in the inset of Fig. 6a. CPE is the constant phase element to account for the depressed semicircle in the experimental spectra. The R_{sf+ct} decreases from 84.05 Ω for the 1st cycle to 41.37 Ω for the 15th cycle, which associates with the activation process of electrode and the formation of SEI film during the initial cycles. After 15 cycles, the resistance of the electrode decreases very slowly and double semicircles appear gradually in the high to medium frequency range (Fig. 6b), suggesting that the surface film (R_{sf}) and charge transfer resistances (R_{ct}) are well separated. These Nyquist plots are fitted with the equivalent circuit shown in the inset of Fig. 6b. The calculated R_{sf} (R_{ct}) in 35th cycle, 60th cycle, 80th cycle, and 100th cycle are 3.35 Ω (32.8 Ω), 3.45 Ω (34.53 Ω), 4.10 Ω (32.80 Ω), and 4.28 Ω (29.17 Ω), respectively. The fitted results are plotted in Fig. S2.† The stable impedance is favorable for elongating the lifetime of a cell, which partly explains the excellent cyclability of the NiO hollow microspheres as shown in Fig. 5c.

The Li^+ diffusion coefficients (D) in the NiO hollow microspheres after different cycles are also estimated according to the following equation:[45]

$$D = \frac{R^2T^2}{2A^2n^4F^4C^2\sigma_w{}^2} \quad (7)$$

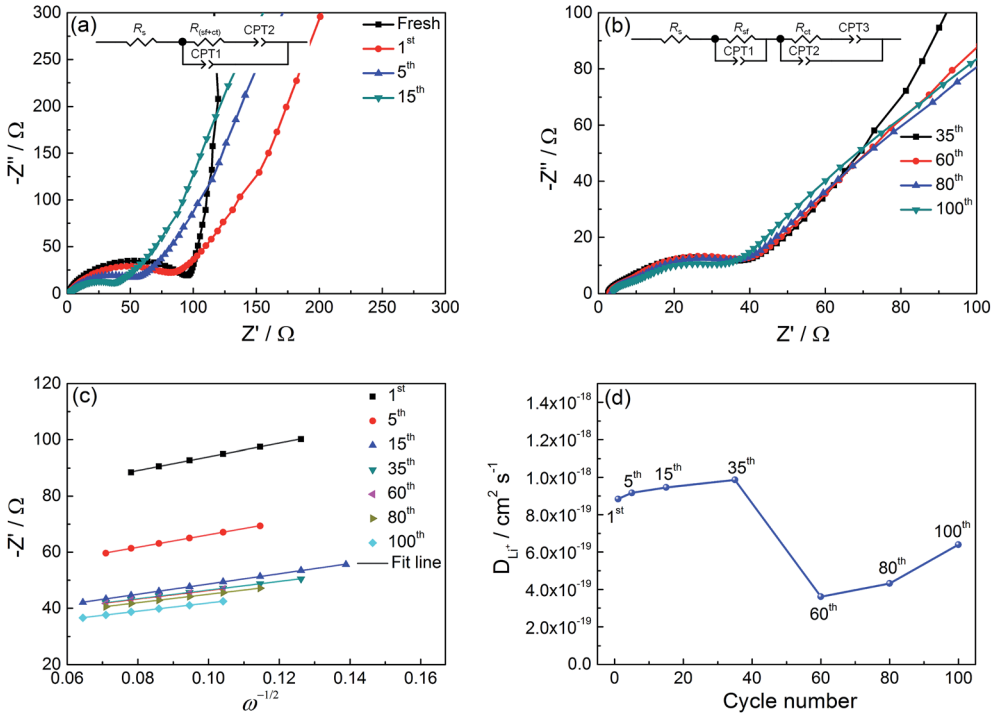

Fig. 6 Nyquist plots of the interconnected nest-like NiO hollow microspheres for (a) the fresh, 1st, 5th and 15th cycle and (b) the 35th, 60th, 80th, 100th cycle with equivalent circuit inset. (c) The relationship between Z' and $\omega^{-1/2}$ at low frequencies. (d) Li^+ diffusion coefficients of the interconnected nest-like NiO hollow microspheres after various discharge/charge cycles.

where R is the gas constant, T is the absolute temperature, A is the surface area of the anode, n is the number of electrons per molecule during cycling, F is Faraday constant, C is the concentration of lithium ion, σ_w is the Warburg factor which can be obtained from the following equation:

$$Z' = R_s + R_{ct} + \sigma_w \omega^{-1/2} \quad (8)$$

where R_s is the resistance of the electrolyte and electrode material, R_{ct} is the charge transfer resistance and ω is the angular frequency in the low frequency region. The relationship plot between Z' and $\omega^{-1/2}$ at low frequency region is shown in Fig. 6c. The result in Fig. 6d calculated by eqn (7) and (8) clearly elucidates that the Li^+ diffusion coefficient for the 1st cycle slightly increases from 8.84×10^{-19} cm^2 s^{-1} to 9.86×10^{-19} cm^2 s^{-1} for the 35th cycle due to the activation process of electrode. After 35 cycles, the Li^+ diffusion coefficient sharply decreases to 3.61×10^{-19} cm^2 s^{-1} for 60th cycle, which can be explained as the stable formation of SEI film resulting in the separation of the surface film resistances (R_{sf}) and charge transfer resistances (R_{ct}) as shown in Fig. S2.†

Generally, the charge storage mechanism of electrode active materials can be classified into components: the faradaic contribution from Li^+ intercalation process and surface capacitive effect (including pseudocapacitance and double-layer capacitance).[46] It has been reported that both the total stored charge and the capacitive contribution to the stored charge increase with decreasing particle size to nanoscale for some metal oxides.[47,48] Since the average size of the primary particles of the NiO hollow microspheres is only ~50 nm, it is very necessary to analyze the capacitive contribution to the total stored charge. Gradually increasing voltammetric scan rates are used to calculate and identify the capacitive contribution as shown in Fig. 7a. According to the analysis proposed by Dunn and coworkers,[49,50] the total current response (i) at a fixed potential (V) can be described as the combination of surface capacitive effect and diffusion-controlled insertion processes (eqn (9) and (10)).

$$i(V) = k_1 v + k_2 v^{1/2} \quad (9)$$

$$i(V)/v^{1/2} = k_1 v^{1/2} + k_2 \quad (10)$$

where $k_1 v$ represents the total surface capacitive contribution, and $k_2 v^{1/2}$ stands for the contribution of the diffusion-controlled insertion process. The linear plot of $i/v^{1/2}$ *versus* $v^{1/2}$ is used to determine k_1 and k_2 as shown in Fig. 7b. Fig. 7c gives a typical separation of the capacitive and diffusion currents at a scan rate of 2.4 mV s^{-1}. The diffusion-controlled insertion processes is mainly occurred at around the peak voltage, indicating that the diffusion process is feasible at this region and corresponds to a redox reaction between Ni^0/Ni^{2+}. Fig. 7d shows the total stored charge due to both diffusion-controlled insertion processes and surface capacitive for LIBs at various scan rates. The diffusion-controlled insertion processes contribution is 58% at 0.1 mV s^{-1} and sharply decreases when increasing scan rate from 0.1 to 5 mV s^{-1}, while the surface capacitive contribution gradually dominates the total capacity and is up to 83% at 5 mV s^{-1}. These

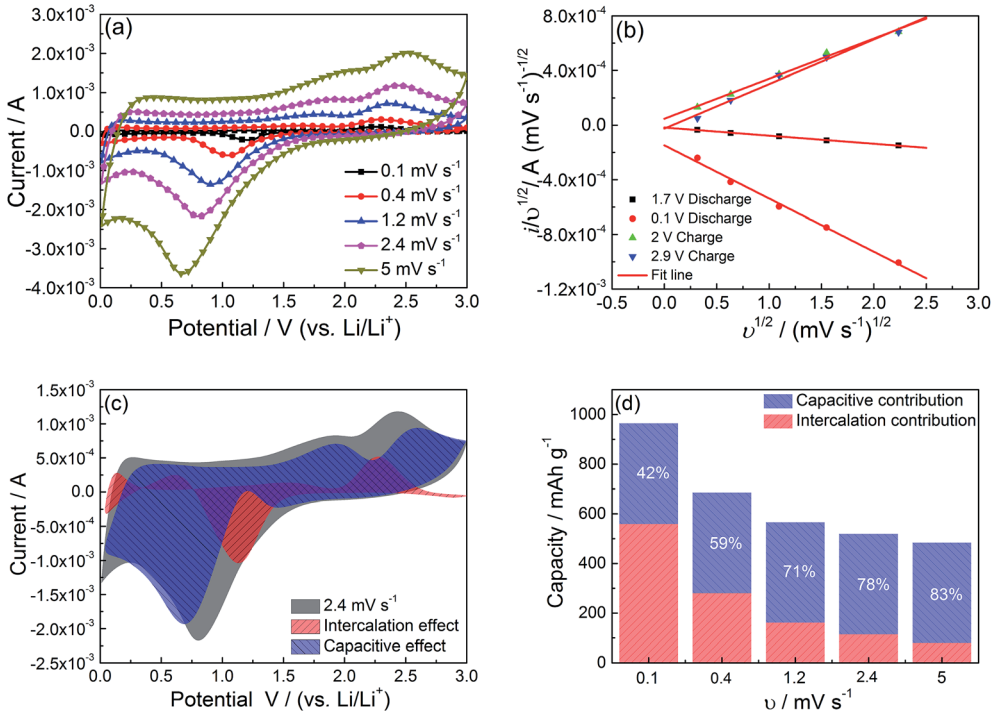

Fig. 7 (a) CV curves of the interconnected nest-like NiO hollow microspheres electrode at different scan rates; (b) the fitted lines of $i(V)/\upsilon^{1/2}$ *vs.* $i/\upsilon^{1/2}$ at different voltage (1.7 V, 0.1 V for cathodic scan and 2 V, 2.9 V for anodic scan); (c) CV curves of the interconnected nest-like NiO hollow microspheres electrode at 2.4 mV s^{-1} (the red and blue shaded portion in the CV plot correspond to intercalation effect and capacitive effect, respectively); (d) capacitive contributions to the total capacity under different scan rates.

results indicate that surface capacitive contribution accounts for a significant proportion of the total capacity, particularly at high scan rates. It is noteworthy that the double layer effect mainly depends on the surface area. However, the surface area of the as-synthesized NiO hollow microspheres is only 7.9 m^2 g^{-1}. Therefore, the great contribution of pseudocapacitive effect to the total stored charge accounts for the excellent high rate capability of the NiO hollow microspheres. These results suggest that the charge stored at the surface of the NiO hollow microspheres from the pseudocapacitance storage mechanism can be a very important factor in achieving high values for the gravimetric energy density.

To ensure the retention of the porous hollow microspheres morphology after cycling, SEM analysis is performed after 80 cycles and 100 cycles at a current density of 1 A g^{-1}. For comparison, the as-prepared NiO hollow microspheres electrode is also subjected for the SEM investigations and obtained image is also presented in Fig. 8. It can be seen that the as-prepared NiO hollow microspheres electrode shows the presence of nest-like hollow microspheres morphology before cycling, indicating the good mechanical strength of this porous hollow microspheres structure (Fig. 8a). After 80 cycles, the porous hollow microspheres structure is well retained except for slight pore expansion (Fig. 8b). After 100 cycles, the complete microspheres structure is difficult to distinguish resulting from the squeeze of separator and the volume expansion during cycling, but the hollow frame is still retained (Fig. 8c). It is noted that the porous hollow structures in the microspheres could improve the structural integrity and accommodate the mechanical strain caused by the volume change during discharge/charge process. Thus, this porous hollow microspheres structure contributes greatly to its superior cycling stability.

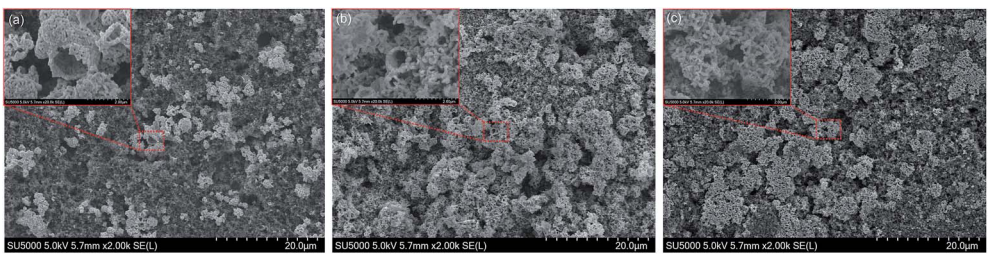

Fig. 8 SEM images of the interconnected nest-like NiO hollow microspheres electrodes (a) before cycling, (b) after 80 cycles, and (c) after 100 cycles.

The superior lithium storage performance of the interconnected nest-like NiO hollow microspheres is believed to be based on their unique architecture resulting from the following aspects: the nano-sized building blocks (very small nanoparticles with diameter around 50 nm) facilitate the transport of both lithium ions and electrons due to the short diffusion length. The mesoporous hollow microspheres structure not only ensures efficient electrolyte penetration and increases the contact area between active materials and electrolyte, but also effectively relaxes the mechanical strain generated upon the discharge/charge cycling. The micro-sized and robust porous hollow microspheres secondary structure can effectively suppress self-aggregation and structural degradation upon cycling. The special interconnected chain-like mesoporous shells can provide a continuous electronic transfer channel and greatly reduce the path lengths of lithium ions diffusion. Moreover, the great contribution of pseudocapacitive charge storage in the discharge/charge process facilitates the improvement of rate capability. The integration of all these advantages enhances the lithium storage performance of the interconnected nest-like NiO hollow microspheres.

4. Conclusions

In summary, interconnected nest-like NiO hollow microspheres were successfully fabricated *via* a facile and cost effective hydrothermal method followed by a simple sintering process. The unique nanoscale characteristics, including interconnected chain-like mesoporous spherical shells, hollow microspheres structure, nanoparticle building blocks, and highly porous structure of these NiO hollow microspheres lead to the superior electrochemical performance in terms of their high lithium storage activity, good cyclability, and excellent rate capability when they are used as a anode active material for LIBs. It delivers a good reversible capacity of 650 mA h g^{-1} after 100 cycles at a current density of 1 A g^{-1} with only 0.07% decay per cycle. When cycled at 5 A g^{-1} and 10 A g^{-1}, it still displays a stable capacity as high as 541 mA h g^{-1} and 457 mA h g^{-1}, respectively. More importantly, computational modeling indicates that the pseudocapacitive effect accounts for a significant portion of the total capacity. The obtained excellent performance, particularly the excellent rate capability associated with pseudocapacitive effect, opens up new opportunities in the development of high performance next-generation LIBs used for alternative energy and electric transportation.

Acknowledgements

The authors thank the financial supports from the National Natural Science Foundation of China (No. 51664012 and 51464009), Guangxi Natural Science Foundation of China (2015GXNSFGA139006), and Innovation Project of Guangxi Graduate Education (YCSW2017158). The authors also thank the supports from Collaborative Innovation Center for Exploration of Hidden Nonferrous Metal Deposits and Development of New Materials in Guangxi.

References

1 S. Shokrzadeh and E. Bibeau, Sustainable integration of intermittent renewable energy and electrified light-duty transportation through repurposing batteries of plug-in electric vehicles, *Energy*, 2016, **106**, 701–711.
2 T. F. Yi, S. Y. Yang and Y. Xie, Recent advances of $Li_4Ti_5O_{12}$ as a promising next generation anode material for high power lithium-ion batteries, *J. Mater. Chem. A*, 2015, **3**, 5750–5777.
3 Y. Hui, L. Y. Cao, Z. W. Xu, J. F. Huang, H. Ouyang and J. Y. Li, Mesoporous $Li_4Ti_5O_{12}$ nanoparticles synthesized by a microwave-assisted hydrothermal method for high rate lithium-ion batteries, *J. Electroanal. Chem.*, 2016, **763**, 45–50.
4 Q. Wang, D. A. Zhang, Q. Wang, J. Sun, L. L. Xing and X. Y. Xue, High electrochemical performances of α-MoO_3@MnO_2 core–shell nanorods as lithium-ion battery anodes, *Electrochim. Acta*, 2014, **146**, 411–418.
5 Y. Zhao, X. F. Li, B. Yan, D. B. Xiong, D. J. Li, S. Lawes and X. L. Sun, Recent Developments and Understanding of Novel Mixed Transition-Metal Oxides as Anodes in Lithium Ion Batteries, *Adv. Energy Mater.*, 2016, **6**, 1502175.
6 L. Pan, X. D. Zhu, X. M. Xie and Y. T. Liu, Smart Hybridization of TiO_2 Nanorods and Fe_3O_4 Nanoparticles with Pristine Graphene Nanosheets: Hierarchically Nanoengineered Ternary Heterostructures for High-Rate Lithium Storage, *Adv. Funct. Mater.*, 2015, **25**, 3341–3350.
7 S. B. Ni, X. H. Lv, J. J. Ma, X. L. Yang and L. L. Zhang, A novel electrochemical reconstruction in nickel oxide nanowalls on Ni foam and the fine electrochemical performance as anode for lithium ion batteries, *J. Power Sources*, 2014, **270**, 564–568.
8 X. L. Sun, W. P. Si, X. H. Liu, J. W. Deng, L. X. Xi, L. F. Liu, C. L. Yan and O. G. Schmidt, Multifunctional Ni/NiO hybrid nanomembranes as anode materials for high-rate Li-ion batteries, *Nano Energy*, 2014, **9**, 168–175.
9 X. L. Sun, C. L. Yan, Y. Chen, W. P. Si, J. W. Deng, S. Oswald, L. F. Liu and O. G. Schmidt, Three-Dimensionally "Curved" NiO Nanomembranes as Ultrahigh Rate Capability Anodes for Li-Ion Batteries with Long Cycle Lifetimes, *Adv. Energy Mater.*, 2014, **4**, 1300912.
10 J. Liang, H. Hu, H. Park, C. H. Xiao, S. J. Ding, U. Paik and X. W. Lou, Construction of hybrid bowl-like structures by anchoring NiO nanosheets on flat carbon hollow particles with enhanced lithium storage properties, *Energy Environ. Sci.*, 2015, **8**, 1707–1711.
11 Y. W. Li, J. H. Yao, E. Uchaker, J. W. Yang, Y. X. Huang, M. Zhang and G. Z. Cao, Leaf-Like V_2O_5 Nanosheets Fabricated by a Facile Green Approach as High Energy Cathode Material for Lithium-Ion Batteries, *Adv. Energy Mater.*, 2013, **3**, 1171–1175.
12 J. H. Liu and X. W. Liu, Two-Dimensional Nanoarchitectures for Lithium Storage, *Adv. Mater.*, 2012, **24**, 4097–4111.
13 L. Zhou, Z. C. Zhuang, H. H. Zhao, M. T. Lin, D. Y. Zhao and L. Q. Mai, Intricate Hollow Structures: Controlled Synthesis and Applications in Energy Storage and Conversion, *Adv. Mater.*, 2017, 1602914.

14 A. Q. Pan, H. B. Wu, L. Zhang and X. W. Lou, Uniform V_2O_5 nanosheet-assembled hollow microflowers with excellent lithium storage properties, *Energy Environ. Sci.*, 2013, **6**, 1476–1479.

15 X. Y. Lai, J. E. Halpert and D. Wang, Recent advances in micro-/nano-structured hollow spheres for energy applications: From simple to complex systems, *Energy Environ. Sci.*, 2012, **5**, 5604–5618.

16 X. H. Huang, J. B. Wu, Y. Lin and R. Q. Guo, NiO Hollow Spheres with Stable Capacity Retention and Enhanced Rate Capability for Lithium Ion Batteries, *Int. J. Electrochem. Sci.*, 2013, **8**, 1691–1700.

17 X. J. Wang, G. Wang, G. H. Zhai and H. Wang, Nickel Oxide Nanoparticle-Assembled Microspheres with a High Rate Capability for Lithium Storage, *Aust. J. Chem.*, 2015, **68**, 964–969.

18 X. Wu, X. An and X. M. Xie, Preparation of $Ni(HCO_3)_2$ and its catalytic performance in synthesis of benzoin ethyl ether, *Trans. Nonferrous Met. Soc. China*, 2014, **24**, 1440–1445.

19 B. B. Wang, G. Wang, X. M. Cheng and H. Wang, Synthesis and electrochemical investigation of core–shell ultrathin NiO nanosheets grown on hollow carbon microspheres composite for high performance lithium and sodium ion batteries, *Chem. Eng. J.*, 2016, **306**, 1193–1202.

20 X. Zhou, S. J. You, X. H. Wang, Y. Gan, Y. J. Zhong and N. Q. Ren, Hydrothermal synthesis of magnetic carbon microspheres for effective adsorption of Cd(II) in water, *J. Appl. Chem. Biotechnol.*, 2014, **89**, 1051–1059.

21 G. X. Zhu, C. Y. Xi, H. Xu, D. Zheng, Y. J. Liu, X. Xu and X. P. Shen, Hierarchical NiO hollow microspheres assembled from nanosheet-stacked nanoparticles and their application in a gas sensor, *RSC Adv.*, 2012, **2**, 4236–4241.

22 T. Wu, Y. Liu, X. Zeng, T. T. Cui, Y. T. Zhao, Y. N. Li and G. X. Tong, Facile Hydrothermal Synthesis of Fe_3O_4/C Core–Shell Nanorings for Efficient Low-Frequency Microwave Absorption, *ACS Appl. Mater. Interfaces*, 2016, **8**, 7370–7380.

23 P. Poizot, S. Laruelle, S. Grugeon, L. Dupont and J. M. Tarascon, ChemInform Abstract: Nano-Sized Transition-Metal Oxides as Negative-Electrode Materials for Lithium-Ion Batteries, *Nature*, 2000, **407**, 496–499.

24 S. J. Hao, B. W. Zhang, S. Ball, B. Hu, J. S. Wu and Y. Z. Huang, Porous and hollow NiO microspheres for high capacity and long-life anode materials of Li-ion batteries, *Mater. Des.*, 2016, **92**, 160–165.

25 H. S. Jadhav, A. K. Rai, J. Y. Lee, J. Kim and C. J. Park, Enhanced electrochemical performance of flower-like Co_3O_4 as an anode material for high performance lithium-ion batteries, *Electrochim. Acta*, 2014, **146**, 270–277.

26 Z. Chen, A. Xiao, Y. Chen, C. Zuo, S. Zhou and L. Li, Template-directed preparation of two-layer porous NiO film *via* hydrothermal synthesis for lithium ion batteries, *Mater. Res. Bull.*, 2012, **47**, 1987–1990.

27 M. Y. Cheng, Y. S. Ye, T. M. Chiu, C. J. Pan and B. J. Hwang, Size effect of nickel oxide for lithium ion battery anode, *J. Power Sources*, 2014, **253**, 27–34.

28 X. Y. Yan, X. L. Tong, J. Wang, C. W. Gong, M. G. Zhang and L. P. Liang, Hydrothermal-synthesized NiO nanowall array for lithium ion batteries, *J. Alloys Compd.*, 2013, **556**, 56–61.

29 F. Cao, G. X. Pan, P. S. Tang and H. F. Chen, NiO nanowall array prepared by a hydrothermal synthesis method and its enhanced electrochemical performance for lithium ion batteries, *Mater. Res. Bull.*, 2013, **48**, 1178–1183.

30 Q. Wang, Y. F. Xu, G. L. Xu, H. Su, S. Y. Shen, T. T. Tu, L. Huang, J. T. Li and S. G. Sun, Synthesis of hierarchical NiO microsphere with waxberry-like structure and its enhanced lithium storage performance, *J. Alloys Compd.*, 2015, **648**, 59–66.

31 X. Chen, N. Q. Zhang and K. N. Sun, Facile ammonia-induced fabrication of nanoporous NiO films with enhanced lithium-storage properties, *Electrochem. Commun.*, 2012, **20**, 137–140.

32 S. Q. Ci, J. P. Zou, G. S. Zeng, Q. Peng, S. L. Luo and Z. H. Wen, Improved electrochemical properties of single crystalline NiO nanoflakes for lithium storage and oxygen electroreduction, *RSC Adv.*, 2012, **2**, 5185.

33 Y. J. Mai, X. H. Xia, R. Chen, C. D. Gu, X. L. Wang and J. P. Tu, Self-supported nickel-coated NiO arrays for lithium-ion batteries with enhanced capacity and rate capability, *Electrochim. Acta*, 2012, **67**, 73–78.

34 C. H. Chen, P. J. Perdomo, M. Fernandez, A. Barbeito and C. L. Wang, Porous NiO/graphene composite thin films as high performance anodes for lithium-ion batteries, *Journal of Energy Storage*, 2016, **8**, 198–204.

35 R. A. Susantyoko, X. H. Wang, Y. Fan, Q. Z. Xiao, E. Fitzgerald, K. L. Pey and Q. Zhang, Stable cyclic performance of nickel oxide–carbon composite anode for lithium-ion batteries, *Thin Solid Films*, 2014, **558**, 356–364.

36 Q. Li, G. Huang, D. M. Yin, Y. M. Wu and L. M. Wang, Synthesis of Porous NiO Nanorods as High-Performance Anode Materials for Lithium-Ion Batteries, *Part. Part. Syst. Charact.*, 2016, **33**, 764–770.

37 M. Y. Cheng and B. J. Hwang, Mesoporous carbon-encapsulated NiO nanocomposite negative electrode materials for high-rate Li-ion battery, *J. Power Sources*, 2010, **195**, 4977–4983.

38 V. Aravindan, P. S. Kumar, J. Sundaramurthy, W. C. Ling, S. Ramakrishna and S. Madhavi, Electrospun NiO nanofibers as high performance anode material for Li-ion batteries, *J. Power Sources*, 2013, **227**, 284–290.

39 C. Wang, D. L. Wang, Q. M. Wang and H. J. Chen, Fabrication and lithium storage performance of three-dimensional porous NiO as anode for lithium-ion battery, *J. Power Sources*, 2010, **195**, 7432–7437.

40 P. P. Lv, H. L. Zhao, Z. P. Zeng, C. H. Gao, X. Liu and T. H. Zhang, Self-assembled three-dimensional hierarchical NiO nano/microspheres as high-performance anode material for lithium ion batteries, *Appl. Surf. Sci.*, 2015, **329**, 301–305.

41 H. W. Lu, D. Li, K. Sun, Y. S. Li and Z. W. Fu, Carbon nanotube reinforced NiO fibers for rechargeable lithium batteries, *Solid State Sci.*, 2009, **11**, 982–987.

42 D. Shao, D. P. Tang, Y. J. Mai and L. Z. Zhang, Nanostructured silicon/porous carbon spherical composite as a high capacity anode for Li-ion batteries, *J. Mater. Chem. A*, 2013, **1**, 15068.

43 J. C. Guo, A. Sun, X. L. Chen, C. S. Wang and A. Manivannan, Cyclability study of silicon–carbon composite anodes for lithium-ion batteries using electrochemical impedance spectroscopy, *Electrochim. Acta*, 2011, **56**, 3981–3987.

44 T. T. Cao, D. Fang, L. Liu, Z. P Luo, Q. Wang, L. J. Dong and C. X. Xiong, Nanosheets-based ZnO–NiO microspheres for lithium-ion batteries, *J. Mater. Sci.*, 2015, **26**, 5279–5286.

45 Z. C. Yan, L. Liu, J. L. Tan, Q. Zhou, Z. F. Huang, D. D. Xia, H. B. Shu, X. K. Yang and X. Y. Wang, One-pot synthesis of bicrystalline titanium dioxide spheres with a core–shell structure as anode materials for lithium and sodium ion batteries, *J. Power Sources*, 2014, **269**, 37–45.

46 T. Brezesinski, J. Wang, J. Polleux, B. Dunn and S. H. Tolbert, Templated Nanocrystal-Based Porous TiO_2 Films for Next-Generation Electrochemical Capacitors, *J. Am. Chem. Soc.*, 2009, **131**, 1802–1809.

47 T. Z. Yuan, Y. Z. Jiang, W. P. Sun, B. Xiang, Y. Li, M. Yan, B. Xu and S. X. Dou, Ever-Increasing Pseudocapacitance in RGO–MnO–RGO Sandwich Nanostructures for Ultrahigh-Rate Lithium Storage, *Adv. Funct. Mater.*, 2016, **26**, 2198–2206.

48 S. Z. Huang, L. Zhang, X. Y. Lu, L. F. Liu, L. X. Liu, X. L. Sun, Y. Yin, S. Oswald, Z. Y. Zou, F. Ding and O. G. Schmidt, Tunable Pseudocapacitance in 3D $TiO_{2-\delta}$ Nanomembranes Enabling Superior Lithium Storage Performance, *ACS Nano*, 2017, **11**, 821–830.

49 J. Wang, J. Polleux, J. Lim and B. Dunn, Pseudocapacitive Contributions to Electrochemical Energy Storage in TiO_2 (Anatase) Nanoparticles, *J. Phys. Chem. C*, 2007, **111**, 14925–14931.

50 L. C. Liu, W. G. Pell and B. E. Conway, Behavior of Molybdenum Nitrides as Materials for Electrochemical Capacitors, *J. Electrochem. Soc.*, 1998, **145**, 1882–1888.